Nanoscale

COMMUNICATION

View Article Online
View Journal | View Issue

Cite this: *Nanoscale*, 2018, **10**, 11737

Received 18th April 2018,
Accepted 13th June 2018

DOI: 10.1039/c8nr03159b

rsc.li/nanoscale

A scalable on-demand platform to assemble base nanocarriers for combination cancer therapy†

Milan Gautam,[a] Sae Kwang Ku,[b] Jong Oh Kim*[a] and Jeong Hoon Byeon *[c]

Chemophototherapy is an advanced cancer therapeutic that uses photothermal nanocarriers (NCs) responsive to near-infrared (NIR) light. For the past decade, chemophototherapy has been investigated intensively for clinical translation, and continuous-flow production of biofunctional compounds (NCs, drugs, probes, nanocomposites) has received increasing attention for future therapeutics. However, *in situ* supply of a stimuli-responsive inorganic core and subsequent tight drug loading on the core are challenging tasks in the practical use of on-demand nanomedicines. Thus, in this study, we designed and evaluated both *in vitro* and *in vivo* models of an aero–hydro–aero single-pass production system for chemophotothermally active NCs. We prepare tightly-drug-loadable cores (titanium peroxide [*y*TiO_2] nanovesicles [NVs]) using hydrogen flame pyrolysis of vaporized $TiCl_4$ (aero) and successive ultrasonic H_2O_2 treatment (hydro). The NVs formed were incorporated with graphene oxide (GO), doxorubicin (D), and polyethylene glycol (P) in a spray to form GO-*y*TiO_2@DP NCs (aero). The NVs' tight DP loading and endothermic effect induced greater, sustained D release and tumor-selective distribution, even for hyperthermic activity. The results showed the route developed may be a stepping stone to scalable, reconfigurable production for on-demand chemophotothermal therapeutics.

Invasive chemical treatments[1–3] have serious side effects, so combination therapies using physical (optical, magnetic, or ultrasonic) stimuli-responsive nanocarriers (NCs) have been intensively investigated to enable better efficacy in cancer therapeutics.[4] In particular, chemophototherapy (combined chemical and photothermal treatments), in which near-infrared (NIR)-induced hyperthermia[5] and burst drug release at tumor sites demonstrate a synergistic effect for cancer treatment,[6,7] has received increasing attention. NCs for chemophototherapy comprise NIR-responsive inorganic cores with clinically-approved drugs and additives (targeting, release control, and/or stealth agents).[8,9] Recently, 2D nanostructures (*e.g.*, graphene oxide [GO], transition metal chalcogenides, black phosphorus) have been used to improve chemophototherapeutic efficacy.[10–12] Among these, due to its abundance and biocompatibility, GO is also considered an efficient vector for proteins,[13] polymers,[14] gene medicines,[15] and probes for bioimaging.[16] Nevertheless, although GO naturally has hydrophilic functional groups on its tips and edges, additional GO surface modification or functionalization for appropriate drug and additive loading is required to achieve efficacy in bioapplications.[17]

A continuous-flow production platform for nanomedicines in a scalable, reconfigurable system, along with the optimum medicine structure design, confers multifunctions on advanced cancer therapeutic carriers. However, the development of the said platform is challenging, especially with regard to a flexible response to changes in industrial demand or the therapeutic regimen.[18] For several years, flow reaction-based continuous production has been used in the preparation of active pharmaceutical ingredients. However, unlike other types of industrial production (*e.g.*, petrochemicals, polymers, food, electronics, and automobiles), batch-by-batch hydrothermal chemistries, purifications, separations, and post-treatments essentially require large facilities and investments, long production times, and costly controls.[19] Recently, multifunctional (*i.e.*, organic–inorganic hybrid) nanocarriers (NCs) have been intensively introduced in cancer therapeutics. In addition, facile or simple preparation platforms based on one-pot or continuous-flow production of multifunctional NCs were tried in order to address the efficacy of NC. The attempts, however, were limited to preparation of core inorganic materials. This shows scalable production of NCs for combination therapy requires a more convoluted platform that combines stimuli-responsive inorganic cores and chemotherapeutic compounds. Rapid NC assembly will lead to substantial advancements in real-time formulation for on-demand, con-

[a]*College of Pharmacy, Yeungnam University, Gyeongsan 38541, Republic of Korea. E-mail: jongohkim@yu.ac.kr*
[b]*College of Korean Medicine, Daegu Haany University, Gyeongsan 38610, Republic of Korea*
[c]*School of Mechanical Engineering, Yeungnam University, Gyeongsan 38541, Republic of Korea. E-mail: postjb@yu.ac.kr*

†Electronic supplementary information (ESI) available. See DOI: 10.1039/c8nr03159b

tinuous-flow production. Several single-pass reaction routes have been introduced for continuous-flow production of NCs for advanced cancer therapeutics; however, because of short processing times, post-treatments with separation or purification (such as chitosan intervention or surface photomodification) are required still upon physical loading of the drug on the core for tight conjugation,[20,21] hindering the realization of on-demand scalable production. To utilize on-demand cancer therapeutics, combining post-treatments to tightly load drugs and other functional compounds in rapid, compact, continuous-flow production is one of the most important tasks. Moreover, practical scalability (*i.e.*, sufficient quantities per day to supply hundreds to thousands of doses) of NCs has not been demonstrated, although enhancing the mass production of newly developed cancer therapeutics is one of the most critical thresholds for process approval. On this account, flame pyrolysis would be a promising continuous supply route of inorganic cores with low cost and high production rate (>g h^{-1}).[22] Nevertheless, conventional flame pyrolysis is only feasible to produce inert inorganic oxide nanoparticles (NPs), which implies that posttreatments are further required to confer binding/adsorbing functions with other functional components; hence, the use of flame pyrolysis is still limited for a wide range of biomedical applications. Consequently, it is highly desirable to conceive versatile, continuous, efficient methodologies for scalable production of multifunctional NCs. A single-pass platform based on aero–hydro (gaseous–aqueous) assembly may be an alternative for scalable, continuous-flow, on-demand production of NCs in a compact, reconfigurable system.

In order to offer a real-time NC formulation platform in this study, we proposed an aero–hydro–aero approach (flame pyrolysis: aero; ultrasonic treatment: hydro; and mechanical spray: aero) to combine titanium peroxide (yTiO$_2$) nanovesicles (NVs) and graphene oxide (GO)-doxorubicin (D)-polyethylene glycol (P) mixture droplets for fresh *in situ* self-assembly of GO-yTiO$_2$@DP NCs without process interruptions (Fig. 1). yTiO$_2$ NVs having net negative surface charges[23] were adopted not only to achieve tight DP loading (model drug with stealth polymer) during the single-pass process through capillary suction (from interparticle voids between primary yTiO$_2$ particles) with adsorption (pores) and electrostatic attraction (insets of Fig. 1)[24] but also to utilize endothermic properties for enhancing hyperthermia.[25] The NCs were sampled directly from the reacted gas flow and dispersed in buffered saline before *in vitro* and *in vivo* cancer chemophototherapy without further purification. By reducing unwanted clearance of hydrophilic DP during delivery, the NCs exhibited greater, sustained D release and tumor-selective distribution compared to GO@DP, suggesting DP is tightly loaded on GO-yTiO$_2$ in a short assembly period (<2 min). In addition, the NCs' photothermal activity was greater than that of GO@DP in both *in vitro* and *in vivo* evaluations. Not only do these findings offer a scalable platform for continuous-flow production of multifunctional NCs, but they also provide a suitable combination for effective cancer chemophototherapy.

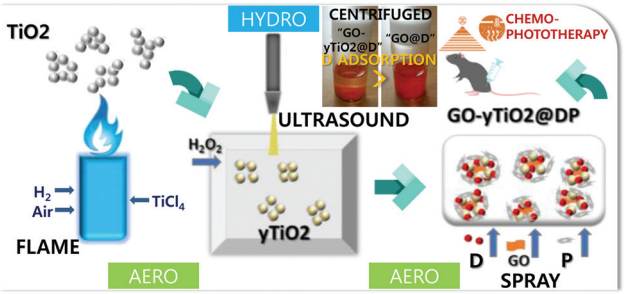

Fig. 1 Schematic of the aero–hydro–aero route to continuously assemble GO-yTiO$_2$@DP NCs. The vaporized precursor from TiCl$_4$ solution bubbling was injected into a hydrogen flame to produce TiO$_2$ NPs, which were then reacted with H$_2$O$_2$ under probe sonication with 1 min residence time. The NPs were hydrosolized, resulting in the continuous formation of yTiO$_2$ NVs. The NVs were then incorporated with GO, D, and P in a nitrogen gas stream to form GO-yTiO$_2$@DP NCs, and the resulting NCs were dispersed in buffered saline for use in chemophototherapy to estimate the efficacy of the NCs and the designed aero–hydro–aero route. Inset: Digital images exhibit tighter D adsorption of GO-yTiO$_2$ than GO.

As shown in Fig. S1 (ESI†), for scalable supply of titania (TiO$_2$) NP precursors, a hydrogen diffusion flame (1.5 L min^{-1} hydrogen, 0.5 L min^{-1} air for TiCl$_4$ vaporization, and 8.0 L min^{-1} air were co-injected into a quartz burner: 141/18/60, Arnold Gruppe, Germany) was used to convert vaporized TiCl$_4$ to TiO$_2$ NPs because flame pyrolysis synthesis of TiO$_2$ is a low-cost, mass-productive aero route.[26] The hydrogen flame-synthesized TiO$_2$ NPs were laden in a gas stream, and the TiO$_2$ flow was injected directly into a reactor with flowing H$_2$O$_2$ solution with probe ultrasonication (20 kHz, 150 W) to form yTiO$_2$ NVs in less than 1 min. The ultrasound probe (VCX 750, Sonics and Materials Inc., USA) was installed inside the reactor, and the direction of ultrasound countered the TiO$_2$ NP-laden flow to collapse the bubbles generated by the flow immediately, resulting in hydrosolization of TiO$_2$ NPs. Next, the reacted solution containing the NVs was aerosolized using a mechanical spray device (lab made, containing a 0.3 mm nozzle) under a pure nitrogen gas flow and entered an activated carbon-silica gel-packed hollow tube to extract residual H$_2$O$_2$. The yTiO$_2$ NV-laden nitrogen flow was used as an operating fluid to spray out GO@DP solution by another spray device in serial connection to generate hybrid droplets. Due to the NVs' adsorption ability and negative surface potential, the NVs were incorporated with GO, and DP was loaded tightly on the NVs in the gas stream. The NVs were subsequently dried by passing droplets through a heated tubular reactor to extract the solvent from the droplets and assemble GO-yTiO$_2$@DP NCs (Fig. S1, ESI†). Since P is known as a colloidal stabilizer in the physiological solutions, we used it as a stealth agent to validate intrinsic tumor accumulation activity of the NCs during blood circulation.[27] The NCs in the gas flow were positively charged through field charging (pin-to-ring corona charger), and the charged NCs were collected directly on a polished duralumin rod (negative potential) in powder form

still in aero-state rod through electrostatic precipitation. The production yield of GO-yTiO$_2$@DP NCs was found to be 1.6 g h^{-1}, which was measured using a piezobalance particle monitor (3522, Kanomax, Japan). To evaluate NCs' performance in chemophototherapy, the rod was immersed finally in buffered saline under bath sonication to prepare NC dispersion before *in vitro* and *in vivo* bioassays without further purification (Fig. 1).

To validate the aero–hydro–aero assembly for preparing GO-yTiO$_2$@DP NCs, we first tried using transmission electron microscopy (TEM; Tecnai G2 F20 S-TWIN, FEI, USA). Fig. 2A shows loosely agglomerated NV structures (46.1 ± 8.1 nm) comprising primary yTiO$_2$ particles (3.9 ± 0.6 nm). Crystalline structure analyses of TiO$_2$ and yTiO$_2$ powder samples using X-ray diffractometry (XRD; D/MAX-2500, Rigaku, Japan) exhibit characteristic peaks of the anatase TiO$_2$ phase, while yTiO$_2$ reveals reduced peak intensities and broadened peak widths (Fig. S2A, ESI†). These results implied H_2O_2 treatment decreases the size of TiO$_2$ NPs *via* ultrasonic homogenization, and the surface crystalline structure is transformed *via* excessive O atoms oriented from hydroxylation.[23,28] Fig. S2A (insert, ESI†) represents this transformation; the digital images show different colors of the powder samples (TiO$_2$: white; yTiO$_2$: yellow). Raman spectra of the samples (XploRA Plus, Horiba, Japan; Fig. S2B, ESI†) show the anatase bands at 391, 512, and 634 cm^{-1}, consistent with XRD measurements,[29] although due to the transformation, there are slight differences in band intensity and position. X-ray photoelectron spectroscopy (XPS; Axis-HIS, Kratos Analytical, Japan) presents two characteristic peaks around at 458.9 and 464.5 eV (with a splitting energy of 5.6 eV) attributed to Ti 2p$_{1/2}$ and Ti 2p$_{3/2}$ spine orbital-splitting photoelectrons, respectively. The O 1s spectra of the yTiO$_2$ sample exhibit more intense characteristic peaks at around 529.8 and 531.5 eV for O^{2-} of the Ti–O bond and O^- of H_2O_2, respectively.[30] This further suggests excessive O atoms on yTiO$_2$ from H_2O_2 treatment and negative surface charges (O_2^{2-}) of yTiO$_2$, as well as differences in Ti 2p doublets between TiO$_2$ and yTiO$_2$. Indeed, Fig. S2C (ESI†) inset tables for the fraction between Ti and O support excess O atoms in yTiO$_2$ than in TiO$_2$. We verified the representative morphology of GO@DP from mechanical spraying (Fig. 2B) as a crumpled structure due to the aero-process and further confirmed the existence of functional groups from GO and DP, such as C=O, COOH, and O–H, through XPS measurements (Fig. S2D, ESI†).[20,31,32] In a previous study, low- and high-magnification TEM images of GO-yTiO$_2$@DP specimens (Fig. 2C) exhibited vesicular structures similar to a functionalized TiO$_2$ nanostructure for anticancer application,[33] and did not show individual GO fragments, suggesting the single-pass process is feasible for producing GO-yTiO$_2$@DP NCs. This suggests also the texture of yTiO$_2$ NVs is workable for tightly combining GO@DP. The high-magnification image reveals d-spacings of 0.366 and 0.338 nm, which matched the (101) plane of anatase TiO$_2$ and the (002) plane of GO, respectively, verifying further the formation of an all-in-one structure from the aero–hydro–aero assembly. Intervening GO between yTiO$_2$ NVs and shattering the agglomerated NVs[34] during mechanical spraying of the mixture solution induce a more uniform distribution than that with yTiO$_2$ alone. In-flight size distributions of undried yTiO$_2$, GO@DP, and GO-yTiO$_2$@DP sprays measured using a scanning mobility particle sizer (SMPS; 3936, TSI, USA) revealed unimodal distributions with greater sizes (Fig. 2D), implying the generated sprays contain each sample without unwanted splitting. Interestingly, the geometric standard deviation (GSD; Table S1, ESI†) of the GO@DP sample was reduced when yTiO$_2$ NVs were included, suggesting DP is tightly adsorbed on the NVs.

We examined the elemental entrapment efficiency (EE) and loading capacity (LC) of D on GO and GO-yTiO$_2$ using ultraviolet-visible (UV-vis) spectrophotometry (U-2800, PerkinElmer, Japan; Fig. S3A, ESI†) before adding P. Higher EE (~100%) and LC (~33%) of D were observed for GO-yTiO$_2$ compared to GO alone (EE: ~86%; LC: ~30%), indicating yTiO$_2$ inclusion can induce tight loading of D. Inclusion of P slightly reduces the analogous values (Fig. 2E), probably due to competitive adsorption between D and P on GO-yTiO$_2$, including the negative potential of P. Nevertheless, the EE and LC results indicated GO-yTiO$_2$ can simultaneously adsorb D and P in the single-pass process. Light absorption spectra of GO@DP and GO-yTiO$_2$@DP samples were analyzed using UV-vis spectrophotometry (Fig. S3B, ESI†). A characteristic absorption band at around 480 nm for D was confirmed at both dispersions,[35] demonstrating D loading further. However, there was no significant difference in NIR absorption between the dispersions, suggesting yTiO$_2$ NVs inclusion does not affect GO's NIR absorption capacity (*i.e.*, GO is mostly incorporated on the surface of each yTiO$_2$ NV). In addition, because of higher D payload, the GO-yTiO$_2$@DP sample exhibited a greater visible light absorption than GO@DP. Fig. S3B (inset, ESI†) shows the different colors of the dispersions, supporting the differences in light absorption spectra. As shown in Fig. S4 (ESI†), dispersion stabilities of GO@DP and GO-yTiO$_2$@DP samples were determined through 1-week monitoring of the hydrodynamic diameter at room temperature using dynamic light scattering (DLS; Nano ZS, Malvern Instruments, UK) on samples dispersed in phosphate-buffered saline (PBS), Dulbecco's modified Eagle's medium (DMEM), and fetal bovine serum (FBS) media. No significant differences among the media were detected during monitoring; however, probably due to agglomeration, slight increases in size were demonstrated over time. The increase detected in GO@DP size was about 30 nm, while the analogous value for GO-yTiO$_2$@DP was about 15 nm, indicating that P's stabilizing activity on GO-yTiO$_2$ is preferable because of tight loading.[36,37] The polydisperse index (PDI) of yTiO$_2$, GO@DP, and GO-yTiO$_2$@DP was 0.19, 0.36, and 0.25, respectively, and these results were consistent with geometric standard deviations (Table S1, ESI†) measured using SMPS. The relatively large PDI of GO@DP could be compensated by incorporating with yTiO$_2$ both in aerosol and hydrosol state. In addition, GO-yTiO$_2$@DP exhibited a modest positive surface charge (+5.7 mV); thus, they were suitable for cellular interaction with minimal cation-mediated cytotoxicity.[38] The sus-

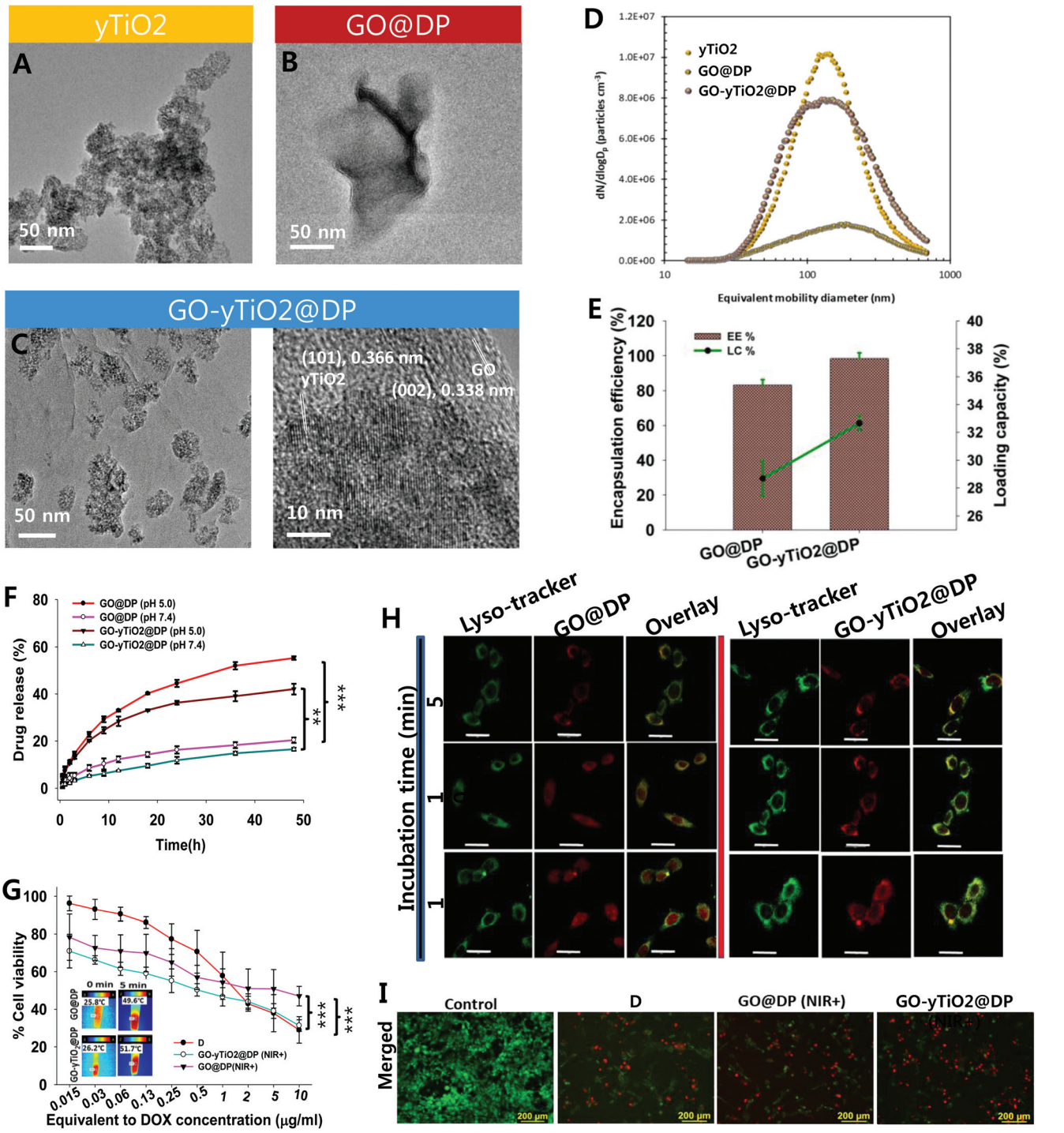

Fig. 2 Characterization and *in vitro* chemophototherapeutic efficacy of GO-yTiO$_2$@DP NCs. TEM micrographs of (A) yTiO$_2$, (B) GO@DP, and (C) GO-yTiO$_2$@DP samples. High-magnification TEM image of GO-yTiO$_2$@DP shows d-spacings of yTiO$_2$ NCs and GO, implying NCs include yTiO$_2$ and GO as a single structure. (D) Particle size distributions of yTiO$_2$, GO@DP, and GO-yTiO$_2$@DP samples in the aerosol state. (E) EE and LC of D on GO@DP and GO-yTiO$_2$@DP. (F) D release profiles from GO@DP and GO-yTiO$_2$@DP at different pH values (**p < 0.01; ***p < 0.001). (G) Cytotoxic responses of SCC-7 cells after treatment with GO@DP and GO-yTiO$_2$@DP with NIR irradiation, including free D (***p < 0.001). (H) Confocal microscope images of GO-yTiO$_2$@DP-treated SCC-7 cells at different time intervals. Lysotracker green was used for tracking lysosomes (scale bar 20 μm). (I) Live and dead images of SCC-7 cells treated with GO@DP and GO-yTiO$_2$@DP with and without NIR irradiation and incubated for 24 h, including free D (scale bar 200 μm).

tained D release from GO-yTiO$_2$@DP NCs was determined using D measurements at different pH (7.4 and 5.0) conditions as a function of diffusion time (Fig. 2F). The NCs exhibited greater sustained D release, even under physiological conditions, because of tight loading of DP, and this effect was more significant at endosomal pH (over half of D in the NCs remained to be released after 48 h). This implies NCs may favor tumor-selective sustained D release for long-term circulation upon their uptake by cancer cells. To induce a safer hyperthermic effect of GO-yTiO$_2$@DP NCs on chemophototherapy, a relatively low NIR irradiation intensity (~2 W cm^{-2}, 808 nm) was adopted to introduce photothermal elevations,[39] and the temperatures were recorded with a thermal camera (Therm-App TH, Opgal Optronic Industries, Ltd, Israel; Fig. S5, ESI†). The dispersion temperature of GO-yTiO$_2$@DP reached 51.7 °C after 5 min NIR irradiation due to π-networks of GO,[40] and was sufficient to have hyperthermic and NIR-triggered D release effects to kill cancer cells synergistically.[21] The temperatures after 3 min irradiation were greater compared to GO@DP, supporting the endothermic effect of yTiO$_2$ NVs further.

We investigated *in vitro* chemophotothermal effects of GO-yTiO$_2$@DP NCs on squamous cell carcinoma-7 (SCC-7) cells and compared them with GO@DP's effects by estimating cytotoxicities using 3-(4,5-dimethylthiazol-2-yl)-2,5-diphenyltetrazolium bromide (MTT) assay. Cytotoxicity estimates of yTiO$_2$, GO, and GO@P (Fig. S6, ESI†) proved the aero–hydro-processed yTiO$_2$ NVs are biocompatible and that slight toxicities of GO can be attenuated further by incorporating P. NIR irradiation onto GO (or GO@P)- and GO-yTiO$_2$ (or GO-yTiO$_2$@P)-treated cells exhibited cell viability reduction in the absence of D because of hyperthermia. The endothermic effect of yTiO$_2$ induced greater cancer cell-killing activity, indicating yTiO$_2$ inclusion can enhance GO's hyperthermic activity. The cell-killing activity of GO-yTiO$_2$@P under NIR irradiation improved further upon D loading for inducing NIR-triggered D release (Fig. 2G). Interestingly, enhanced hyperthermia due to greater temperature elevation of GO-yTiO$_2$@DP NCs (Fig. 2G insets) revealed greater cell-killing activity than GO@DP, even under NIR irradiation, although the cumulative D release from GO@DP was greater than NCs at both pH values. This suggests using proper phototherapeutic NCs might induce greater efficacy in cancer treatment, even at low D doses. We addressed the internalization of GO@DP and GO-yTiO$_2$@DP into SCC-7 cells using confocal laser scanning microscopy (CLSM; K1-Fluo, Nanoscope System, Inc., Korea) and fluorescence-activated cell sorting (FACS; BD Bioscience, USA) analyses. The confocal images (Fig. 2H) show GO@DP was highly uptaken inside the nucleus (red fluorescence) after 15 min, probably due to rapid D release outside the cells from destabilized GO@DP in the extracellular environment. On the other hand, GO-yTiO$_2$@DP NCs co-localized in the lysosomes, where the lysosomal environment (pH 4.5–5.0) was suitable for D release inside the cells through cancer-selective uptake due to tight loading of stealth P. No significant D fluorescence signals at the nucleus suggest because of their stability, NCs do not exhibit abrupt D release inside the cells.[41] FACS supports NC stability, consistent in both a time- and a concentration-dependent manner (Fig. S7A†). Furthermore, live/dead assay was used to confirm the *in vitro* efficacy of GO-yTiO$_2$@DP NCs in chemophototherapy (Fig. 2I). Fig. S7B† shows separated live and dead cell images. Likewise in MTT assay, upon NIR irradiation, the fraction of dead cells for NCs was greater than for GO@DP and comparable with free D because of the combined therapeutic effect that can accelerate cellular apoptosis.[42]

In order to study the practical use of aero–hydro–aero assembly, we investigated the antitumor efficacy of NCs in an *in vivo* mice model. To evaluate biodistribution, we conjugated GO@DP and GO-yTiO$_2$@DP samples with a cyanine5.5 (Cy5.5) fluorescent probe (Fig. 3A). Although the NCs were not additionally treated for tumor targeting, the NC-administered mice model exhibited significant fluorescence signals on the tumor site 6 h postinjection, while limited signals were found in GO@DP-treated mice. With time, Cy5.5 accumulation in the tumor site in NC-treated mice increased progressively, and the final Cy5.5 fluorescence intensity was significantly greater compared to GO@DP-treated mice (Fig. 3B) *via* its decrease in the heart, kidneys, and lungs with time. The low tight loading property of single-pass-assembled GO@DP may result in rapid D clearance due to tissue distribution, although P coexists. This shows D circulation improvement, as well as D accumulation on the tumor site *via* the enhanced permeability and retention (EPR) effect, can be achieved by involving tight P loading, demonstrating superior therapeutic activity over the free drug.[43] The GO@DP- and GO-yTiO$_2$@DP-administered SCC-7 tumor-bearing xenograft mice were exposed to NIR laser for 5 min to confirm *in vivo* photothermal activity (Fig. 3C). The final temperature of the tumor mass in GO-yTiO$_2$@DP-treated mice postirradiation was higher than in GO@DP-treated mice, and the difference between GO@DP and GO-yTiO$_2$@DP was greater compared to *in vitro* measurements, probably due to higher accumulation of GO-yTiO$_2$@DP on the tumor site, considering *in vivo* biodistribution results.

When the tumor ~100 mm^3 in size, SCC-7 tumor-bearing xenograft mice were divided randomly into six groups (G1–G5) and treated with GO@DP and GO-yTiO$_2$@DP with and without NIR irradiation, including free D. Tumor volumes and body weights of the mice were monitored for 24 days, and the normalized volumes and weights were plotted as a function of time (Fig. S8A and S8B, ESI†). During the 24 days, no mice died. Free D-treated mice experienced simultaneous tumor growth and weight loss in the early stage of treatment, but there were no significant changes in body weight in the other mice, suggesting mice tolerate P-included samples quite well without any systemic toxicities. The reduction in tumor volumes from NIR-irradiated configurations was comparable, and the greatest reduction was seen in GO-yTiO$_2$@DP NC-treated mice. This was visually confirmed by digital images of the tumors (Fig. 3D). After 12 days of NC treatment, only small black scars remained on the tumor site, and these reduced further by day 24, leaving a negligible tumor mass, while in

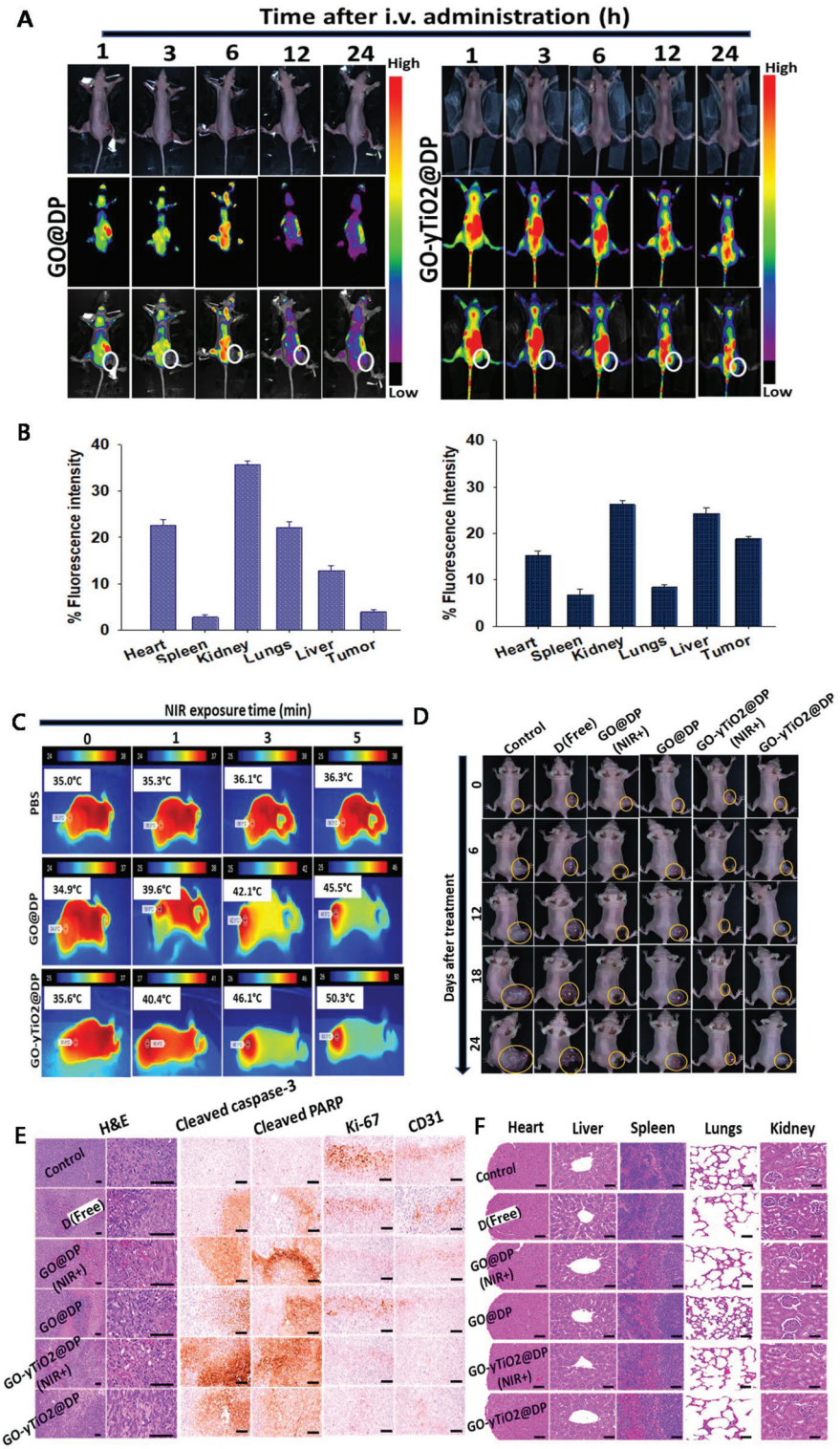

Fig. 3 *In vivo* biodistribution and antitumor studies of GO@DP and GO-*y*TiO_2@DP. (A) Biodistribution contours (circles represent tumor regions) and (B) fluorescence intensity profiles of Cy5.5-loaded GO@DP and GO-*y*TiO_2@DP in major organs and tumors of SCC-7 tumor xenograft mice. (C) Photothermal imaging upon NIR irradiation (0–5 min) on tumors in GO@DP- and GO-*y*TiO_2@DP-treated mice, including normal saline. (D) Digital images of tumor-bearing mice (circles represent tumor regions) after treatment with GO@DP and GO-*y*TiO_2@DP with and without NIR irradiation, including free D. (E) Hemotoxylin and eosin (H&E) and immunocytochemically stained tumor sections (cleaved caspase-3, cleaved PARP, Ki-67, and CD31) and (F) histopathological images of mice post-treatment with GO@DP (G3 with NIR, G4) and GO-*y*TiO_2@DP (G5 with NIR, G6) with and without NIR irradiation, including untreated (G1) and free D-treated (G2) mice. Scale bars 120 μm.

GO@DP-treated mice, slight tumor regrowth was detected after 18 days of treatment. Interestingly, no NIR irradiation treatment (*i.e.*, GO@DP and GO-*y*TiO_2@DP) also exhibited greater tumor reductions compared to free D treatment, probably due to stealth P loading, which reduces potential adverse effects of D.[44]

To determine the expression levels of cleaved caspase-3, cleaved poly(adenosine diphosphate [ADP]-ribose) polymerase (PARP), Ki67 (tumor proliferation marker), and CD31 (angiogenesis marker) (Fig. 3E; summarized in Table S2, ESI†), histopathological and immunohistochemical analyses of the tumors were conducted. Treatment using GO-*y*TiO_2@DP NCs exhibited high expression of apoptotic markers, cleaved caspase-3, and PARP compared to GO@DP, including free D; therefore, low expression was observed for Ki67 and CD31. These results supported the enhanced tumor accumulation of tightly-DP-loaded configurations further and were intensified upon NIR irradiation due to synergistic therapeutic effects. The systemic toxicities of GO-*y*TiO_2@DP NCs were analyzed by pathological examinations and compared with GO@DP and free D (Fig. 3F; summarized in Table S3, ESI†). We found no noticeable histopathological signs in the heart, liver, spleen, lungs, and kidneys of all the treated-mice compared to the control mice. From these assessments, we concluded single-pass-assembled NCs may be a suitable platform for chemophototherapies. This presents possibilities of further enhancement in cancer therapeutics by combining NCs with other functional compounds, such as targeting agents and tumor receptors. We further performed a hemolytic study (Fig. S8C and S8D, ESI†) on GO@DP and GO-*y*TiO_2@DP samples (5 μg mL^{-1} equivalent to D). The results revealed GO-*y*TiO_2@DP induces the lowest hemolytic activity compared to GO@DP and free D. The tightly loaded P on GO-*y*TiO_2 could significantly decrease the hemolytic toxicity of D, indicating including *y*TiO_2 can also lead to enhanced hemocompatibility.

The reconfigurable production of this approach was validated by employing a small scale reactor (12 mg h^{-1} capacity) or a different flame pyrolysis (using two precursors, gold[III]–chloride hydrate and zinc naphtenate, instead of titanium[IV] chloride). The small reactor produced GO-*y*TiO_2@DP (Fig. S9A, ESI†) with 56.4 nm of average hydrodynamic diameter and 0.23 of PDI, which were comparable with those from the present (large) reactor. Injecting the two precursors instead of $TiCl_4$ into hydrogen flame produced Au–ZnO NPs, and these NPs were incorporated with GO and DP at a mechanical spray device likewise GO-*y*TiO_2@DP formation. This process finally produced GO-Au-ZnO@DP NCs with 78.8 nm of average hydrodynamic diameter and 0.26 of PDI, demonstrating the reconfigurable production of base NCs.

Conclusions

This study discussed the development of a continuous, scalable route to produce tightly-drug-loadable photoresponsive NCs *via* single-pass aero–hydro–aero assembly of GO-*y*TiO_2@DP NCs to demonstrate its efficacy in chemophototherapy and rapid production. Not only did we attempt to construct a continuous, scalable production platform but we also designed a novel NC structure for suitable drug-photosensitizer combinations in a single-pass configuration. We adopted hydrogen flame pyrolysis as a tool for industrial-scale production to supply TiO_2 NPs for deriving tightly-D-loadable *y*TiO_2 NVs through single-pass ultrasonic H_2O_2 treatment; hence, the GO-*y*TiO_2@DP NCs were appropriately assembled in less than 2 min after spray incorporation with GO, D, and P components. The essential properties of NCs, such as pH selectivity for sustained D release, stealth property for tumor accumulation, and photothermal activity for hyperthermia, were examined in both *in vitro* and *in vivo* models without the use of additional functional compounds (targeting and/or release control agents) in order to validate NCs' efficacy as a practical platform for chemophototherapy. Core *y*TiO_2 NVs enhanced sustained D release and tumor-selective distribution of GO@DP, as well as photothermal temperature elevation, although the NCs did not contain additional release control and tumor-targeting agents. Inclusion of *y*TiO_2 NVs into GO@DP induced tight loading of DP, and the endothermic effect of phototheramally generated heat exhibited greater synergistic anticancer activity under NIR irradiation with minimum side effects than *y*TiO_2-absent configurations (GO@DP, free D). The results suggested NCs from a single-pass continuous-flow platform confer functions for tight loading of DP. This innovative design to prepare multibiofunctional NCs may appeal to a broad readership and holds immense promise for realizing on-demand, continuous-flow production of nanomedicines in a scalable, reconfigurable system for a broad range of cancer therapeutics. These findings, stemming from aero–hydro–aero assembly of tightly-drug-loadable and photostimulatable NCs, may not only offer a reliable base material for chemophototherapy but also provide significant insights into the scalability of multibiofunctional NCs for built-to-order therapeutics.

Conflicts of interest

There are no conflicts to declare.

Acknowledgements

This research was supported by the Medical Research Center Program (2015R1A5A2009124) through the NRF funded by MSIP. This work was also supported by the 216A580056 Yeungnam University Research Grant.

Notes and references

1 Z. Zhang, J. Wang and C. Chen, *Adv. Mater.*, 2013, **25**, 3869.
2 Y. Min, C.-Q. Mao, S. Chen, G. Ma, J. Wang and Y. Liu, *Angew. Chem., Int. Ed.*, 2012, **51**, 6742.

3 X. Xu, W. Ho, X. Zhang, N. Bertrand and O. Farokhzad, *Trends Mol. Med.*, 2015, **21**, 223.
4 J. Shi, L. Wang, J. Zhang, R. Ma, J. Gao, Y. Liu, C. Zhang and Z. Zhang, *Biomaterials*, 2014, **35**, 5847.
5 J. P. May and S.-D. Li, *Expert Opin. Drug Delivery*, 2013, **10**, 511.
6 T. S. Hauck, T. L. Jennings, T. Yatsenko, J. C. Kumaradas and W. C. W. Chan, *Adv. Mater.*, 2008, **20**, 3832.
7 J. H. Byeon and Y.-W. Kim, *Small*, 2014, **10**, 2331.
8 C. Hong, J. Kang, H. Kim and C. Lee, *J. Nanosci. Nanotechnol.*, 2012, **12**, 4352.
9 X. Wang, Y. Liu, Z. Liu, J. Hu, H. Guo and F. Wang, *Biochem. Biophys. Res. Commun.*, 2018, **495**, 867.
10 M. Li, Z. Luo and Y. Zhao, *Chem. Mater.*, 2018, **30**, 25.
11 J. R. Choi, K. W. Yong, J. Y. Choi, A. Nilghaz, Y. Lin, J. Xu and X. Lu, *Theranostics*, 2018, **8**, 1005.
12 P. Zhang, C. Hu, W. Ran, J. Meng, Q. Yin and Y. Li, *Theranostics*, 2016, **6**, 948.
13 M. Dowaidar, H. N. Abdelhamid, M. Hällbrink, X. Zou and Ü. Langel, *Biochim. Biophys. Acta*, 2017, **1861**, 2334.
14 M. Alibolandi, M. Mohammadi, S. M. Taghdisi, M. Ramezani and K. Abnous, *Carbohydr. Polym.*, 2017, **155**, 218.
15 H.-C. C. Foreman, G. Lalwani, J. Kalra, L. T. Krug and B. Sitharaman, *J. Mater. Chem. B*, 2017, **5**, 2347.
16 B. Murugesan, J. Sonamuthu, N. Pandiyan, B. Pandi, S. Samayanan and S. Mahalingam, *J. Photochem. Photobiol., B*, 2018, **178**, 371.
17 S. Shi, F. Chen, E. B. Ehlerding and W. Cai, *Bioconjugate Chem.*, 2014, **25**, 1609.
18 A. Adamo, R. L. Beingessner, M. Behnam, J. Chen, T. F. Jamison, K. F. Jensen, J.-C. M. Monbaliu, A. S. Myerson, E. M. Revalor, D. R. Snead, T. Stelzer, N. Weeranoppanant, S. Y. Wong and P. Zhang, *Science*, 2016, **352**, 61.
19 P. J. Kitson, G. Marie, J.-P. Francoia, S. S. Zalesskiy, R. C. Sigerson, J. S. Mathieson and L. Cronin, *Science*, 2018, **359**, 314.
20 R. K. Thapa, J. H. Byeon, S. K. Ku, C. S. Yong and J. O. Kim, *NPG Asia Mater.*, 2017, **9**, e416.
21 B. K. Poudel, J. O. Kim and J. H. Byeon, *Adv. Sci.*, 2018, **5**, 1700563.
22 D. O. Raemy, R. N. Grass, W. J. Stark, C. M. Schumacher, M. J. D. Clift, P. Gehr and B. Rothen-Rutishauser, *Part. Fibre Toxicol.*, 2012, **9**, 33.
23 M. Pacia, P. Warszyński and W. Macyk, *Dalton Trans.*, 2014, **43**, 12480.
24 K. C.-W. Wu, Y. Yamauchi, C.-Y. Hong, Y.-H. Yang, Y.-H. Liang, T. Funatsu and M. Tsunoda, *Chem. Commun.*, 2011, **47**, 5232.
25 W. Lin and C. J. Murphy, *ACS Cent. Sci.*, 2017, **3**, 1096.
26 A. J. Gröhn, S. E. Pratsinis, A. Sánchez–Ferrer, R. Mezzenga and K. Wegner, *Ind. Eng. Chem. Res.*, 2014, **53**, 10734.
27 X. Sun, Z. Liu, K. Welsher, J. T. Robinson, A. Goodwin, S. Zaric and H. Dai, *Nano Res.*, 2008, **1**, 203.
28 G. Zhang, F. Fan, X. Li, J. Qi and Y. Chen, *Chem. Eng. J.*, 2018, **331**, 471.
29 T. Ohsaka, F. Izumi and Y. Fujiki, *J. Raman Spectrosc.*, 1978, **7**, 321.
30 X. Kong, C. Zeng, X. Wang, J. Huang, C. Li, J. Fei, J. Li and Q. Feng, *Sci. Rep.*, 2016, **6**, 29049.
31 P. Wang, Z.-G. Liu, X. Chen, F.-L. Meng, J.-H. Liu and X.-J. Huang, *J. Mater. Chem. A*, 2013, **1**, 9189.
32 B. Konkena and S. Vasudevan, *J. Phys. Chem. Lett.*, 2012, **3**, 867.
33 M. Nakayama, R. Sasaki, C. Ogino, T. Tanaka, K. Morita, M. Umetsu, S. Ohara, Z. Tan, Y. Nishimura, H. Akasaka, K. Saito, C. Numako, S. Takami and A. Kondo, *Radiat. Oncol.*, 2016, **11**, 91.
34 J. H. Byeon and J. T. Roberts, *ACS Appl. Mater. Interfaces*, 2012, **4**, 2693.
35 L. Zeng, Y. Pan, Y. Tian, X. Wang, W. Ren, S. Wang, G. Lu and A. Wu, *Biomaterials*, 2015, **57**, 93.
36 M. Paola, D. Franco and C. Luigi, *Curr. Drug Metab.*, 2012, **13**, 105.
37 W. Zhang, Y. Wang, X. Sun, W. Wang and L. Chen, *Nanoscale*, 2014, **6**, 14514.
38 E. Fröhlich, *Int. J. Nanomed.*, 2012, **7**, 5577.
39 J. T. Robinson, S. M. Tabakman, Y. Liang, H. Wang, H. S. Casalongue, D. Vinh and H. Dai, *J. Am. Chem. Soc.*, 2011, **133**, 6825.
40 B. Tian, C. Wang, S. Zhang, L. Feng and Z. Liu, *ACS Nano*, 2011, **5**, 7000.
41 E. R. Gillies and J. M. Fréchet, *Bioconjugate Chem.*, 2005, **16**, 361.
42 M. S. Khan, S. Pandey, M. L. Bhaisare, G. Gedda, A. Talib and H.-F. Wu, *Colloids Surf., B*, 2017, **160**, 543.
43 J. Ding, M. Feng, F. Wang, H. Wang and W. Guan, *Oncol. Rep.*, 2015, **34**, 1825.
44 S. Zhu, M. Hong, G. Tang, L. Qian, J. Lin, Y. Jiang and Y. Pei, *Biomaterials*, 2010, **31**, 1360.